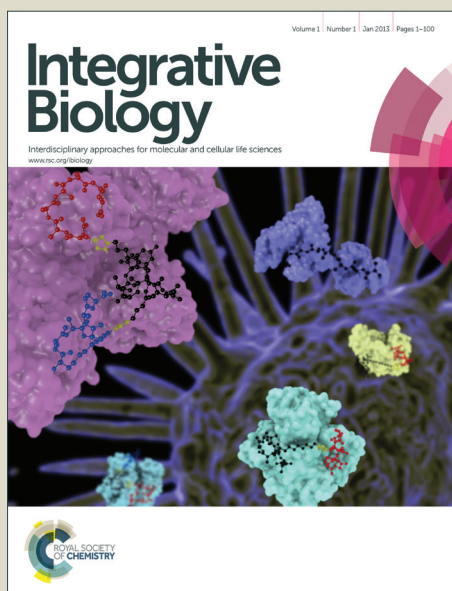


Integrative Biology

Accepted Manuscript



This is an *Accepted Manuscript*, which has been through the Royal Society of Chemistry peer review process and has been accepted for publication.

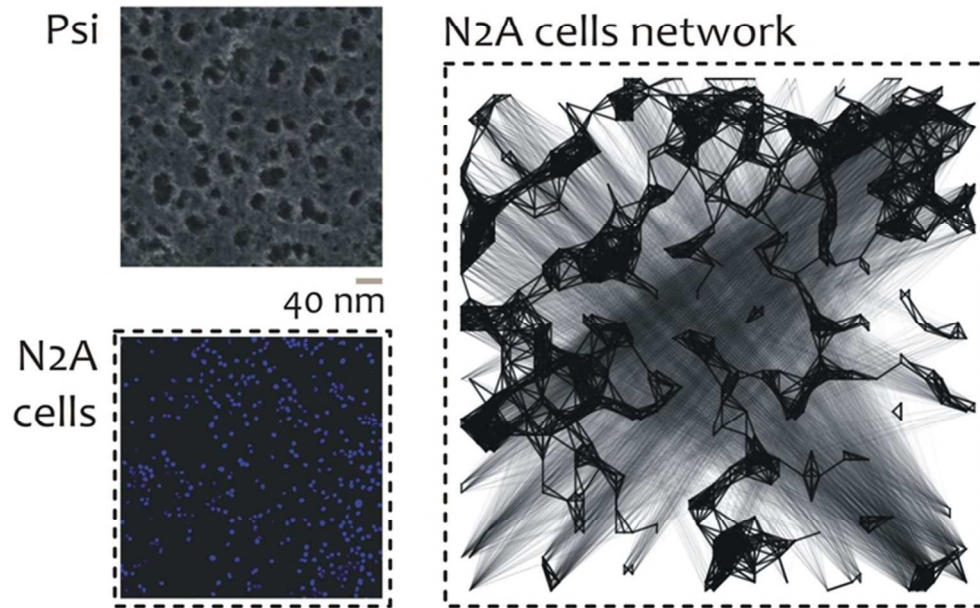
Accepted Manuscripts are published online shortly after acceptance, before technical editing, formatting and proof reading. Using this free service, authors can make their results available to the community, in citable form, before we publish the edited article. We will replace this *Accepted Manuscript* with the edited and formatted *Advance Article* as soon as it is available.

You can find more information about *Accepted Manuscripts* in the [Information for Authors](#).

Please note that technical editing may introduce minor changes to the text and/or graphics, which may alter content. The journal's standard [Terms & Conditions](#) and the [Ethical guidelines](#) still apply. In no event shall the Royal Society of Chemistry be held responsible for any errors or omissions in this *Accepted Manuscript* or any consequences arising from the use of any information it contains.

This work combines nanotechnology, biology and network analysis tools to understand the propensity of neurons to form complex networks. We utilized nano-fabrication techniques to realize porous silicon substrates in which the pore size is in the small nano-meter range. We used the described substrates to analyze the effect of a nano-geometry on the adhesion and organization properties of neural cells in comparison to nominally flat substrates. We observed that neural cells on the porous substrates create highly clustered, small world topology patterns. We conjecture that neurons with a similar architecture may elaborate information more efficiently than in random or regular grids.

N2A cells on porous substrates create
small world topology patterns



N2A cells on porous substrates create highly clustered, small world topology patterns.
63x50mm (300 x 300 DPI)

Networks of Neuroblastoma Cells on Porous Silicon Substrates Reveal a Small World Topology

Giovanni Marinaro^{1,2}, Rosanna La Rocca¹, Andrea Toma¹, Marianna Barberio³, Laura Cancedda¹, Enzo Di Fabrizio^{4,5}, Paolo Decuzzi^{1,5,6} and Francesco Gentile^{7,5,1,†}

¹ Istituto Italiano di Tecnologia, Via Morego 30, 16163 Genova, Italy

² European Synchrotron Radiation Facility, CS40220, 38043 Grenoble Cedex 9, France

³ Department of Physics, Università della Calabria, Via P. Bucci 33c, 87036 Rende, Italy

⁴ King Abdullah University of Science and Technology, Thuwal 23955-6900, Saudi Arabia

⁵ Department of Experimental and Clinical Medicine, University of Magna Graecia, 88100 Catanzaro, Italy

⁶ Department of Nanomedicine, The Methodist Hospital Research Institute, Houston, Texas 77030 – USA

⁷ Department of Electrical Engineering and Information Technology, University of Naples, 80125, Naples, Italy

† *author to whom correspondence should be addressed: gentile@unicz.it*

The human brain is a tightly interweaving network of neural cells where the complexity of the network is given by the large number of its constituents and its architecture. The topological structure of neurons in the brain translates into its increased computational capabilities, low energy consumption, and nondeterministic functions, which differentiate human behavior from artificial computational schemes. In this manuscript, we fabricated porous silicon chips with a small pore size ranging from 8 to 75 nm and large fractal dimensions up to $D_f \sim 2.8$. In culturing neuroblastoma N2A cells on the described substrates, we found that those cells adhere more firmly and proliferate on the porous surfaces compared to conventional nominally flat silicon substrates, that were used as a control. More importantly, we observed that N2A cells on the porous substrates create highly clustered, small world topology patterns. We conjecture that neurons with a similar architecture may elaborate information more efficiently than in random or regular grids. Moreover, we hypothesize that systems of neurons on a nano-scale geometry evolve in time to form networks in which the propagation of information is maximized.

Key Words: porous silicon, small world networks, neural networks, nano-topography, fractal dimension, cell adhesion, free energy principle.

Introduction

The human brain contains an extraordinary number of neuronal cells of diverse types (i.e. on the order of 10^{12}), the complexity of human behavior depends less on the specialization of individual nerve cells and more on the fact that a great many of these cells form complex networks¹.

Neurons are specialized, adherent, electrically excitable cells which have the function to process and transmit information through electrical and chemical signals^{1,2}. While the behavior of individual neurons has been extensively investigated, when a large number of these neurons forms 2 or 3 dimensional architectures unexpected properties may arise, which are not explicable in terms of simple components. This is a typical example of a complex physical system, in which interactions among a large number of elements yield collective phenomena with improved abilities in contrast to isolated components of that system³⁻⁵. A fundamental understanding of how individual neurons interact to form (perhaps hierarchical) clusters, and how the topology of these networks affect the quality, density and spread of information throughout the network, may help to elucidate the mechanisms through which the brain marshal its millions of individual nerve cells to produce behavior, and how are these cells influenced by the environment¹. This theme is attracting increasing interest and may be the key to understand the human brain and its diseases and ultimately to emulate its computational capabilities⁶.

Neurons, like the large majority of cells, can sense and respond to a wide range of external signals, both chemical and physical, and, on integrating and analyzing this information, they can change their morphology, dynamics and organization. The adhesion, growth, migration, differentiation of neural cells is regulated by the response to environmental signaling, and this encompasses a wide range of physical cues that are generated at, or act on, the adhesive interface between cells and the surrounding matrix. Transmembrane adhesion receptors of the integrin family are responsible for the described processes⁷⁻⁹. *Focal adhesions* comprehend integrin-based molecular complexes which are sensitive to, and may recognize, the biochemical characteristics of the substrate, as well as its rigidity and spatial organization. These are dynamic actin–integrin links, the formation and maturation of which are driven by feedback from spatial and temporal interactions between the actin cytoskeleton, and are present in the periphery of cells in the form of flat, elongated structures. Differently from focal adhesions, *focal complexes* are the earliest microscopically visible integrin containing structures, which appear as spots with

diameter ranging from ~100 nm down to ~30 nm or less⁸. Therefore, geometries with details in the low nanometer range may affect and guide the organization of neuronal cells on a substrate. Thus, *nanotechnology* may provide instruments to understand how the cellular sensory machinery interacts with extremely small cues to regulate adhesion and migration, and to explore strategies to obtain neuronal networks with the desired characteristics. As for some examples, using anisotropic gratings in the sub micrometric range, in which the spacing of the gratings was varied over a significant range, Ferrari et al demonstrated the nano-topographic control of neuronal polarity¹⁰; using either gratings and ordered arrays of pillars Ankam et al proved how the size and spacing of these features would determine the fate of human embryonic stem cells to neuronal or glial lineage¹¹; using a variety of different substrate preparations, ranging from islands of carbon nanotubes to posts, ridges or pillars, to randomly rough surfaces, research groups worldwide demonstrated independently that topographic cues at the nano-scale may direct, control and, in some cases, improve neuronal adhesion¹²⁻¹⁵, growth¹⁶, differentiation^{17, 18}, organization or self-organization into simple to complex networks¹⁹⁻²³, electrical signaling²⁴.

In few cases, the adhesive behavior of neuroblastoma N2A cells was verified over porous silicon with a fixed²⁵ or smoothly variable pore size²⁶. Recalling that, according to the IUPAC definition²⁷, surfaces with a pore size smaller than 2 nm, comprised between 2 and 50 nm, and larger than 50 nm, are categorized as micro-porous (MiP), meso-porous (MeP) and macro-porous (MaP) silicon, respectively, results presented in^{25, 26} indicate that nerve cells are sensitive to nano-scale surface topography with feature sizes smaller than 20 nm, that is, in the MeP regime. Porous silicon is promising smart material obtained from bulk silicon through well assessed electrochemical procedures. The size and shape and distribution of the holes in the porous matrix can be finely adjusted on changing few parameters of the fabrication process, including the etching time, current intensity, active etchant concentration, temperature of the process^{25, 28}. The growing interest in porous silicon (PSi) for several biomedical applications is justified by its distinctive attributes that include, but are not limited to, biodegradability under physiological conditions²⁷, biocompatibility^{29, 30}, hydrophobicity²⁸, photoluminescence³¹ properties. For all this, porous silicon has been utilized for fabricating smart devices for a variety of applications including the controlled release of drugs³², for the separation from serum of the low molecular weight content for spectroscopic and spectrometric analysis^{33, 34}, for orthopedic implants.

In this manuscript, using electrochemical methods described in [Fig.1](#) and in the Materials and Methods, we realized porous silicon chips with a small pore size ranging from 8 to 75 nm (that is, in the MeP and MaP regimes) and large fractal dimensions up to $D_f \sim 2.8$. Moreover, using the described substrates, we assessed the ability of porous silicon to boost the assembly of neuroblastoma N2A cells into highly clustered networks in comparison to unetched silicon, that was used as a control. Results indicate that porous silicon substrates with a large fractal dimension promote the formation of *small world* topology patterns of N2A cells. It is hypothesized that neurons in a network with a similar topology may transmit information more efficiently than those left free to evolve over simple unconstrained surfaces.

Results

Fabrication and characterization of the porous silicon substrates. Two different topologies of porous silicon were obtained, namely (i) MaP silicon with an average pore size S of $S \sim 75$ nm, and (ii) MeP silicon. In the case of MeP silicon, the pore dimension was finely adjusted to have an average pore size in the low MeP regime, that is $S \sim 8$ nm; and an average pore size in the intermediate MeP regime, that is $S \sim 18$ nm. In the following, we shall indicate with *small pore* MeP (SP MeP) silicon the first configuration, and with *large pore* MeP (LP MeP) silicon the second configuration.

Several SEM micrographs of the MaP substrates were taken over different samples to assess uniformity and reproducibility. [Fig.2a-b,c](#) reproduce SEM micrographs of a MaP surface taken at different magnifications ranging from $10\ 000\times$ ([Fig.2a](#)) to $100\ 000\times$ ([Fig.2d](#)). The morphological details of the porous surface are more clearly revealed in [Fig.2e](#) which represents an ultra-high magnification image of the inset in [Fig.2d](#). The described ultra-high resolution SEM images have a sufficient level of detail to allow a precise evaluation of the pore size distribution in the macro-porous regime, that is, for pores larger than 50 nm, even without the need of adsorption/desorption isotherms. From these and other similar images, using image analysis algorithms described in previous works²⁵, we derived the pore size distribution as reported in [Fig.2i](#). The pores size S varies around the average value $S \sim 75$ nm with a small standard deviation $\sigma \sim 5$ nm, which confirms the uniformity of the pores over the substrate with

few pores below the 50 nm limit. In addition to this, the SEM image in **Fig.2b** reveals the thickness t of the porous matrix in the silicon substrate that, for particular subset of parameters used here, is about $t=250$ nm (that is, from 3 to 4 times the average pore size). Additional SEM images of the pore substrates are conveniently included in a separate **Supporting Information file #1** to further verify the pore size distribution. The topology of the macro-porous silicon matrix was further verified through AFM imaging, as in **Fig.2f,g**. From this, using algorithms thoroughly described in³⁵ a power spectrum was derived (**Fig.2h**) and used to estimate the effective fractal dimensionality D_f of the substrate that reads $D_f \sim 2.7$, which is very close to the value $D_f \sim 2.8$ found for a meso-porous architecture as in^{25,28}. The fractal dimension is an index for characterizing fractal patterns by quantifying their complexity as a ratio of the change in detail to the change in scale, therefore, it can be used to describe intimately the topography of a variety of systems at the smaller scales. In this case, a high degree of fractality, compared to the $D_f \sim 2.2$ of an unmodified flat silicon substrate²⁵ and to the value $D_f = 2$ of an ideal Euclidian surface, indicates that the surface reveals a hierarchical structure which bridges the micro and nano scales, and this may be responsible²⁸ for the artificial, increased hydrophobicity of the sample exhibiting a contact angle of $\theta \sim 120^\circ$ (**Fig. 1.l**) and this status is generally preserved for a few days after fabrication. Differently, the Si substrate is hydrophilic with a contact angle $\theta = 60^\circ$. For our specific purposes, the PSi substrates were oxidized post fabrication thus providing a hydrophilic surface with contact angles of $\theta \sim 35^\circ$ (**Fig. 1.m**).

The MeP silicon substrates were characterized similarly. The small pore configuration is investigated in **Fig.3a,b**, where the SEM micrograph in **Fig.3a** and the AFM profile in **Fig.3b** do both confirm that the average pore size S is $S \sim 8$ nm with a standard deviation $\sigma \sim 4$ nm.

Differently, the large pore MeP silicon exhibits a larger $S \sim 18$ nm pore size ($\sigma \sim 5$ nm) and this is confirmed by the SEM and AFM images reported in **Fig.3d-e**. The pore size distributions for the small and large pore size silicon patterns are reported in **Fig.3g** for direct comparison. The AFM profiles of the substrates were further processed to determine the corresponding power spectrum density functions (**Fig.3c,f**) using the methods described above and in the Materials and Methods. From these, the fractal dimensions of the surfaces were determined being $D_f \sim 2.8$ for the SP MeP architecture, and $D_f \sim 2.5$ for the LP MeP surface. Contact angle measurements of the samples upon heating show that the substrates are rendered hydrophilic with a contact angle of

$\theta \sim 31^\circ$ (Fig.3.m) that is similar to that derived for the MaP architecture. And thus the surface energy is comparable for all the porous substrates that is to say that differences in cell adhesion and networking may be ascribed to the geometry of the substrates solely.

Cell Adhesion and Proliferation on MaP Silicon Substrates. The described porous substrates were used for verifying the ability of nano-sized geometries to guide cell growth and adhesion in comparison to nominal flat surfaces (that are, the unmodified silicon substrates). Notice that a similar analysis is here conducted on the MaP silicon substrates solely to confirm and expand the adhesion behavior of N2A cells on MeP surfaces already obtained from the same authors of the present paper and reported in ²⁵.

Neuroblastoma cells were incubated over fragments of silicon substrates ($\sim 15 \times 15$ mm) and at different time points, namely 24, 36, 48, and 60 h, the silicon substrates were first washed to remove loosely adhering and death cells; then, the remaining cells were fixed and labeled with DAPI. The cells adhering within a region of interest (ROI) of $\sim 1 \times 1$ mm² were counted using fluorescent microscopy following the procedure described in the Materials and Methods. For each substrate, more than 40 ROIs were considered to provide a meaningful sample size for statistical analysis. The number of adhering cells per unit surface is shown in Fig.4a as a function of time and in Fig.4b as a function of sample preparation. It may be observed that the number of cells increases with time for the porous substrate and is practically constant for the flat silicon substrate, used as a control. Moreover, the number of adhering cells is significantly larger on the porous substrate for all the considered time points. Taken together, the diagrams in Figure 4 demonstrate that the adhesion and growth of N2A cells is accelerated on a porous substrate in opposition to the development of N2A cells in standard conditions, where standard conditions are herein embodied by a nominal flat surface. This experimental evidence supports the notion that cells preferentially adhere and grow over substrates with a nanometer architecture rather than on flat Si substrates, possibly because those samples have a large fractal dimension well in line with the results obtained in precedent works^{25, 36}.

Topological properties of Networks of N2A on the PSi substrates. Fig.5a is a confocal image of the nuclei of neuroblastoma cells (which are stained with DAPI and thus appear in blue) over a flat silicon substrate taken 36 h after incubation. Similarly, Fig.5d represents a confocal image of an ensemble of N2A cells cultured over a MaP silicon substrate and acquired at the same time

point $t=36$ h. In the following, we shall call *nodes* the centers or nuclei of the cells (these are, the components of the circuit), which interact through *edges* that connect pairs of those nodes (these are, the interactions of the circuit). Also, sometimes we may use interchangeably the terms *network* or *graph* to indicate a set of nodes and corresponding edges in a plane. The images are disposed one above the other in the panel of **Figure 5** for direct comparison. From this, it may be deduced that the cells over a non-corrugated Si substrate are distributed apparently randomly in the plane. Differently, neuroblastoma cells over a MaP Si substrate have the propensity to organize to form few, highly clustered groups of individual cells. The corresponding graphs are reported as **Figures 5 b** (flat Si substrate) and **e** (MaP Si substrate). In the first graph (flat Si substrate), the edges are distributed uniformly in the ROI, in opposition to this, in the second graph (MaP Si substrate) one can notice the emergency of connections either (i) within the groups (intra-group interactions) and (ii) between the groups (inter-group interactions). This is further evidenced in the diagrams reported in **Figure 5 c** and **f**, in which the frequency distribution of nodal distances in a network is represented for the flat Si (**c**) and MaP Si (**f**) substrates. In the first diagram, the distribution can be fitted by a Gaussian function, where the average value of the function is the average distance between the nodes (that is here expressed in pixels). In the second diagram, the nodal distances distribution resembles a bimodal function, in which the first peak corresponds to the average distance between the nodes in a group (average intra-nodal distance), and the second peak corresponds to the average distance between groups of nodes (average inter-group distance).

The Gaussian one peaked function that describes the nodal distances in the flat silicon instance, may be a distribution that minimizes the free energy content of N2A cells on flat silicon, in this case the individual cell configuration dominates over the organization of cells in clusters and thus the single N2A cell is the stable element. Differently, in the nano-scale porous case, the system is maintained in a state of lowest energy by a bimodal distribution, whereby the stable element in the system is a group or cluster of cells that is therefore the stable element. We may review these findings on saying that in the first case (that is, the flat silicon substrate) the elementary block of the system is the cell, in the second case (that is, the nano structured porous surface) the elementary block is the cluster of cells.

The observation that cells on a *porous* surface create clusters of cells in opposition to *flat* silicon in which they are instead uniformly distributed, here reported for the MaP silicon configuration, is a general result that was likewise recorded for the SP and LP MeP architectures. In the [Supporting Information file #2](#), we include similar examples of N2A cells wiring diagrams derived on SP and LP MeP silicon substrates, and these reveal the same behavior described for the MaP structure.

Even if we seeded the same amount of cells on both surfaces at the initial time (see the Materials and Methods), maybe because flat silicon presents less anchorage points with respect to modified porous silicon, cell density on flat silicon after 24 hours is largely reduced. To surpass this limitation, we performed additional experiments, herein reported, in which the initial cell density on flat silicon is artificially augmented from 3 to 5 times the initial value (from $\sim 10^5$ cells per substrate up to $\sim 5 \times 10^5$ cells per substrate). In doing so, we could compare the behavior of N2A cells on different substrates (that are, flat and porous) at the same *effective* cell density (that is about 200 to 400 cells/mm², see also [Figure 4](#) in the main text). The corresponding N2A cells wiring diagrams, and the distributions of the number of edges of these diagrams (that are single peaked) are reported in the [Supporting Information Figures S3.1,2](#) and confirm the behavior of neural cell on the surface is not influenced by cell density. The propensity of cells to form complex patterns is thus regulated by the sole substrate topography, that is a notable result.

The described diagrams represent examples extracted from a significantly larger set of data. These suggest that a porous architecture may boost the spontaneous organization of neuroblastoma cells into clustered networks. This hypothesis was verified through an analysis of the data on a statistical basis. Confocal images of the cells over the substrates were analyzed per each substrate preparation and for all the considered time points using the methods described in the Materials and Methods. The clustering coefficient C_c and the characteristic path length C_{pl} , derived as a function of time for the silicon and porous substrate, are shown in [Fig.6a](#) and [b](#). These are two parameters that are widely used to describe the topological properties of a graph. The clustering coefficient describes the propensity of the nodes of a graph to form few groups in which the elements of the groups are inter-connected by the an elevated number of edges³⁷⁻³⁹. The clustering coefficient ranges between 0 and 1 and is here averaged over all nodes of a graph to yield a global clustering parameter. The characteristic path length is the shortest path between

a generic couple of nodes averaged over all pairs of nodes in a graph³⁹. It is generally greater than 1 and indicates the number of steps that on average separates two nodes randomly taken in the network. The reader may find in the Materials and Methods and in the [Supporting Information file #4](#) an operational definition of these two parameters.

The bar chart in [Fig.6a](#) indicates that the cells incubated on the porous substrates exhibit a clustering coefficient which varies over the interval $\sim 0.3 - \sim 0.7$, differently, cells incubated on the flat silicon surface exhibit a lower clustering coefficient that does not exceed 0.05, the observed difference between flat and porous silicon substrates is statistically significant ($p < 0.05$) for all the time points considered in the analysis. The data presented in the diagram indicate that cells deposited on the porous substrates tend to cluster together differently from the cells on a simple flat silicon surface.

Similarly, the diagram in [Fig.6b](#) shows that cells on porous silicon substrates have a low Cpl ranging from 2 to 4, while neuroblastoma cells on flat silicon reveal higher values of Cpl that may reach and surpass 10. And thus, networks of N2A cells on a substrate modified at the nano-scale (that are, the porous silicon substrates) have preferential routes of communication between nodes of the network (which are *closer*) in comparison to networks of N2A cells on a regular smooth surface (that is, the flat Si substrate), in which instead nodes are *farther*. Similarly to the case of Cc, the difference between the Cpl coefficients derived for the porous and flat Si substrates is statistically significant ($p < 0.05$) for all the considered time frames in the analysis. The complete sets of wiring diagrams of N2A cells on the nano structured porous surfaces and flat silicon for all the times of the analysis are reported in the [Supporting Information file #5](#) and [#6](#), respectively.

The spatial invariance of the un-modified flat silicon with respect to porous silicon may explain the observed propensity of neuroblastoma cells to form organized structures on a nano-scale surface (that are, the porous silicon substrates) in opposition to a nominally flat surface (that is, the un-modified silicon substrate). On a porous surface with pores in the nanometer range, neuronal like cells with their filipodia are stimulated to sense and explore their nearest surroundings and migrate until they may find, interact and connect to other cells to form hierarchical clusters of those cells. Differently, on flat, low fractal dimension surfaces the anchorage points are strongly reduced, cells with their filipodia can sense no differences in the

external environment and a similar absence of information variation on small scales may prevent their migration.

Possibly more important than this, in the present study we demonstrate that, depending on the substrate preparation, the nuclei of the cells are displaced to occupy precise positions in the plane. That is, the cells reproduce specific patterns. The reason why those cells form some patterns and disregard other geometries is, at the present, still matter of debate. We may assume that the main drivers for neural cells organization in the plane are the following: (i) *energy optimization*, whereby (neural) cells create networks which minimize energy consumption; (ii) *information propagation*, and thus cells on a substrate form networks through which the information propagation is maximized; (iii) *neural morphogenesis*, the positions of the cells on the substrate is dictated by the morphology of neurons and synaptic connections on that substrate. And thus we may have 3 different criteria which regulate cells networking, and namely the energy criterion, the information criterion, the biology (or evolution) criterion. It is reasonable to speculate that the above criteria are not independent, and that the cells fate is dictated by a (perhaps non-linear) balance of energy, information, biology. Provided that the described mechanisms should be investigated independently with experiments, if proved correct this hypothesis would reveal itself an *unprecedented* tool for neural analysis, in that it would state the equivalence between energy, information theory and biology. And thus, making experiments or studies in one of those fields, one would obtain information in the remaining. An example of this is represented by the observation that, in determining the positions of the nuclei in the plane (that is maybe governed by an *information principle*, and this shall be largely discussed in the following of the paper), one could predict the actual synaptic connections length upon cell differentiation.

Discussion

In the present study we used N2A neuroblastoma cells that is a cell line derived from a brain tumor, in contrast to primary neuronal cultures. This choice is justified by convenience, ease of use, availability. The statistically significant number of experiments allowed to extend the generality of our results. It is known⁴⁰ that neuroblastoma cell lines express neuronal and neuroendocrine properties. One of the hallmarks of neuroblastoma cells in culture is their

spontaneous or induced elaboration of neuritic processes. Moreover, those cell lines possess diverse neuronal properties, including: the synthesis of neurotransmitter biosynthetic enzymes; expression of neurofilaments; opioid, muscarinic and neurotrophin receptors expression; dense core granules presumed sites of catecholamine storage; immunoreactivity to neuron specific enolase⁴⁰. In addition to this, the ability of neuroblastoma cell lines to differentiate in response to a variety of biologic response modifiers has led to the use of neuroblastoma cell lines as model systems to study neuronal and neuroendocrine cell development⁴⁰. Differentiation includes elaboration of extensive neuritic processes that are ultrastructurally and electrophysiologically similar to normal neurons. For all this, a N2A neuroblastoma cell line may represent a simpler model of a primary neuronal cells culture, and still not that coarse to miss to capture or reflect some of the most salient features and biologically relevant aspects of primary neurons.

Taken together, the diagrams in **Figure 6** indicate that N2A cells on a surface modified at the nano-scale, that are the porous silicon substrates, have an increased ability to create patterns in which the nodes of the patterns form highly clustered groups (large Cc) and the elements of the groups are connected by a finite, and generally low, number of steps (small Cpl), in contrast to a nominally flat surface. This is even more evident in the scatter plots in **Figures 7 a to d**, where the Cc and Cpl values of N2A cells on the porous and flat silicon surfaces are reported in an individual diagram at diverse time frames and this permits to visualize at a glance the differences between the described substrates. In a Cc-Cpl plane, the cells on the porous substrates and those on a flat silicon substrate are described by sets of points that are separated and occupy different regions of the plane, and the described difference is even more pronounced with time (you may interpret this like: the systems evolve towards a position of equilibrium with time, we shall discuss later what the physical meaning of such a status may be). Cells on the porous substrates are confined in the upper left region of the diagram, while cells on a flat silicon substrate are confined in the lower right side of the diagram (minor differences in the position between groups of cells on the porous surfaces can be ascribed to the different fractal structure of MaP, SP and LP MeP silicon, that is reflected by their fractal coefficients that are, respectively, $D_f \sim 2.7$, $D_f \sim 2.8$, $D_f \sim 2.5$, and that are generally larger than that revealed by flat silicon, that is $D_f \sim 2.3$). This is an interesting result *per se*, in that shows that the topography of a substrate affects the network anatomy of an ensemble of N2A cells that interact with that substrate. Nevertheless, it

deserves to be debated even further. Consider the diagram in [Fig.7e](#). This is a conceptual scheme built after the fundamental works of Watts and Strogatz^{5, 41, 42}, Amaral and colleagues⁴³ and references therein. It tells us that it is possible to categorize classes of networks on the basis of the two clustering coefficient and characteristic path length parameters solely. Regular ordered networks have elevated clustering coefficients and characteristic path lengths, on the contrary, random graphs possess low clustering and short paths. More interestingly, there exists a third class of complex graphs that lies between the extremes of order and randomness^{3, 5}: *small world* networks exhibit short paths and high clustering, similar networks are named small world in analogy with the concept of small world phenomenon developed in social psychology⁴⁴. N2A cells on porous substrate meet these requirements, therefore they belong to the class of small world networks. (Of course, the definition of a small world network is a little bit more rigorous than this discursive thesis. With Watts and Strogatz⁴², a graph Λ with a specific C_c and C_{pl} shares the properties of a small world network if $C_c \gg C_r$ and $C_{pl} \sim C_{pl_r}$, where C_r and C_{pl_r} are the clustering coefficient and characteristic path length of a random network with the same number of nodes and edges of Λ . In a separate [Supporting Information file #5](#), we provide evidence of this. The C_c and C_{pl} values of a randomly generated set of graphs are reported for comparison with the networks of N2A cells on the porous substrates. This proves mathematically the initial hypothesis that cells on a porous surface reveal a small world topology. In the [Supporting Information file #6](#), for comparison, we include the networks of N2A cells on flat silicon for all the times of the analysis).

Small world networks have recently attracted much attention and examples of small world networks have been studied or documented in a variety of fields ranging from cell biology and neuroscience⁴⁵⁻⁴⁷, to theoretical virology⁴⁸, to dynamical systems⁴⁹, to the study of connections in the world wide web and social networks^{44, 50}. This fame is no surprise for two reasons: (i) the study of networks pervades all of science and (ii) the structure influences function. The intuition of Watts and Strogatz was that dynamical systems with short paths and high clustering may feature enhanced signal propagation speed and computational capabilities compared to regular grids of the same size. In small world networks, the spread of information may be extremely efficient⁴⁴ and this could impact significantly the understanding, design or realization of artificial, biological, or hybrid neural networks, in which the quality, quantity and density of

information throughout those networks is largely increased in comparison to conventional lattices.

The main results of this research are that the geometry of substrate (with a nanometer porous architecture) influences the networking properties of N2A cells in a plane and, specifically, it shapes cell graphs to have improved small world characteristics. Notice though that the present study is based on a preliminary topological analysis: it indicates where and how the cells are positioned in a plane, and it suggests that a similar arrangement may positively influence the communication among neurons, yet it gives limited information on the effective signaling coupling of those neurons.

The effective readout of neural signaling in a network, and to which extent this signaling is affected by the architecture of the substrate, remains a fundamental goal, to afford which more *sophisticated* approaches are required, and are therefore left for future work. These approaches may include, but are not restricted to, high-speed functional multineuron calcium imaging (fMCI), large-scale synapse mapping, and multiple whole-cell and dynamic patchclamp recording techniques⁵¹. Moreover, in analyzing how signals propagate in a lattice of (perhaps randomly distributed) neurons, extra mathematical models are required and should be refined, which are, pairwise spike correlations for determining the surprise index in a network, the study and improvement of information theory mathematical tools, and the correlation between entropy and information in neural networks^{52,53}. Indeed, information theory quantifies how much information a neural response carries about the stimulus. This can be compared to the information transferred in particular models of the stimulus–response function and to maximum possible information transfer.

Consider now the work of the physics and neuro-scientist Karl Friston. In⁵⁴ he proposes a free-energy principle whereby biological systems (differently from other purely deterministic systems), and ultimately the brain apparatus, tend to maintain a state of high order: they tend to minimize the entropy content of the system sometimes violating the second law of thermodynamics and the fluctuation theorem⁵⁵. Moreover, in the Supplementary Information of the cited Review, he demonstrates the equivalence between the free energy principle and the infomax principle. This *maximum information preservation* principle, introduced by Linsker⁵⁶,

states that the signal transformation that is to be realized at each stage of a system is one that maximizes the information (the Shannon information rate) that the output signal values convey about the input signals values, subject to certain constraints and in the presence of processing noise. In the framework of the information theory applied to neuroscience, we may therefore tempt a very simple interpretation of the presented results. Nanometer cues on a surface (and these may be a nano-porous architecture or other), that are incidentally in the same order of magnitude of the mechanosensing machinery of neural cells, elicit the self-organization of those cells in a fashion that the propagation of information throughout the network is maximized.

Also notice that the porous substrates used in the present study exhibit scale dependent relationships and a large fractal dimensions ranging from $D_f \sim 2.5$ for the LP MeP architecture, to $D_f \sim 2.7$ for MaP silicon, to $D_f \sim 2.8$ for the SP MeP structure, in contrast to $D_f \sim 2.3$ derived for flat silicon. Interestingly, the human cerebral cortex has a similar value of fractal dimensions $D_f \sim 2.8$ and this reflects its complexity and self-similar nature⁵⁷. On these basis, we may therefore better expand or argument the preceding hypothesis: on interacting with a substrate, N2A cells (and perhaps neurons) in a network form small world patterns (that is equivalent to say, they assume a conformation that maximizes the information rate throughout the network) if and only if the geometry of the substrate has a sufficiently high degree of complexity, i.e., a large fractal dimension (that is the value of complexity towards which brain has evolved⁵⁷). This would explain why, differently from porous substrates, smooth silicon chips do not stimulate N2A cells to build efficient networks.

If proved correct, this understanding could help to elucidate the mechanism that regulate the ways the human brain works, moreover, it may be used to design advanced circuits with the ability to break otherwise computationally intractable problems.

Conclusions

We fabricated porous silicon chips with a small pore size ranging from 8 to 75 nm and large fractal dimensions up to $D_f \sim 2.8$. In seeding neuroblastoma cells over similar substrates, we found that adhesion of those cells is enhanced in contrast to nominally flat silicon substrates. More importantly, we found that those cells on porous surfaces display high clustering and short paths,

that typically characterize small world networks. Based on these data, it can be speculated that neurons with a similar topology may transmit and process information more efficiently than in conventional architectures. Moreover, we hypothesize that nano-sized geometries may elicit the spontaneous evolution of a system of nerve cells towards networks in which the spread of information throughout those networks is maximized.

Materials and Methods

Fabrication of the porous substrates. Porous silicon (PSi), is a form of Si containing a layer of nano sized pores artificially introduced in its microstructure, thus revealing an increased surface to volume ratio. PSi exhibits promising properties including highly controllable and reproducible pore size and distribution; bioreactivity; biocompatibility; biodegradability in physiological environment; hydrophobicity. Here, three different porous substrates were prepared, and namely (i) macro porous (MaP) silicon substrates with an average pore size larger than 50 nm, (ii) small pore meso porous (SP MeP) silicon substrates with an average pore size of 8 nm and (iii) large pore meso porous (LP MeP) silicon substrates with an average pore size of 18 nm.

Porous silicon was prepared via a porosification process as described, for instance, in²⁷, and here recapitulated for sake of clarity. Porous silicon substrates were generated from a bulk boron-doped p-type (100) silicon wafer via anodization. The original silicon wafer was placed in a teflon electrolytic cell where a platinum cathode and the silicon wafer (anode) are immersed in a hydrogen fluoride (HF) solution (**Fig.1**). Substrates with various pore sizes were obtained by tailoring the etching conditions, that are the intensity of etching current, the concentration of HF solution, and the length of process.

The wafers were cleaned with acetone and ethanol to remove possible contaminant and then etched with a 4% wet HF (by Carlo Erba) solution. Therefore, they were rinsed with water and dried with N₂. MaP silicon substrates were obtained by Si anodization, using an electrolyte mixture of HF, D.I. water and DMF (by Sigma-Aldrich) (9:1:115, v/v/v). A constant current density of 4 mA/cm² was applied for 4 min at 25 °C. SP MeP substrates were obtained by Si anodization using an electrolyte mixture of HF, D.I. water, and ethanol (by Sigma-Aldrich) (1:1:2, v/v/v). A constant current density of 20 mA/cm² for 5 min at 25 °C was applied. LP MeP

substrates were obtained using a constant current density of 4 mA/cm² for 5 min at 25 °C. In this case, an electrolyte mixture of HF, D.I. water, and methanol (by Sigma-Aldrich) (5:3:2, v/v/v) was used. In doing so, thin porous layers are obtained over the original flat substrate with a thickness of a few tens of microns. The samples were finally rinsed in D.I. water, ethanol, and pentane with 4 minutes steps. The PSi substrate were finally oxidized in oven at 200 °C for 2 hours.

Atomic Force Microscopy characterization of the samples. Atomic force microscopy (Veeco MultiMode with NanoScope V controller) was used for the measurement and characterization of the MaP structures. All the measurements were performed in a dry environment in intermittent contact mode over a sampling area of 500×500 nm². Room temperature was hold fixed for all the acquisitions. Ultra-sharp Si probes (ACLA-SS, AppNano) with a nominal tip radius less than 5 nm were used for achieve high resolution. Multiple measurements were done in different scan directions to avoid artefacts. At least four images in height mode (trace and retrace) were recorded per sample. The images had a resolution of 1024×1024 points and were acquired at a scanning rate of 1 Hz. The obtained images were processed with the WSxM® software, using either flattening or plane fit according to the relief characteristics, with the minimal polynomial order needed. The characteristic average surface roughness (R_a) was thus deconvoluted for each substrate. Using conventional mathematical procedures implemented in Mathematica®, a power spectrum (PS) was further derived for each image which, in turn, was used to derive the fractal dimension of the substrates, as explained in the following.

SEM characterization of the samples. SEM images of the porous substrates were captured using a Dual Beam (SEM-FIB) - FEI Nova 600 NanoLab system. During acquisition, the beam energy and the corresponding electron current were fixed to 15 keV and 0.14 nA, respectively. The nano-porous morphology was imaged by employing the mode 2 configuration, whereby images can be magnified over 2500×10³ magnifications and ultra-high resolution can be achieved.

Surface contact angle measurement. Surface hydrophilicity of the samples was determined by measuring the water contact angle with one drop of about 5 µl of D.I. water using an automatic contact angle meter (KSV CAM 101, KSV Instruments LTD, Helsinki, Finland) at room

temperature. Four measurements were performed on each substrate to evaluate the average contact angle θ , at 5 s.

Fourier analysis and fractal dimension of the substrates. The AFM profiles were processed to obtain the corresponding Power Spectrum density functions $C(q)$ of the samples²⁸:

$$C_{2D}(q) = \frac{1}{(2\pi)^2} \int \langle z(\chi)z(o)e^{-iq\chi}d\chi^2 \rangle \quad (1)$$

where $\chi=(x, y)$ is the planar coordinate; $z(\chi)$ is the surface profile measured from the average surface plane, defined as $\langle z \rangle = 0$; and q is the wave number, related to the characteristic wavelength λ as $q=2\pi/\lambda$. The symbol $\langle \dots \rangle$ stands for ensemble averaging over a collection of different surfaces with identical statistical properties. Since Eq.(1) is bidimensional, it is impractical for comparison purposes, for this, a more convenient 1D power spectrum density, $C(q)$, is further derived using the FACA (Fractal Analysis by Circular Averaging) approach, being

$$C(q) = \frac{1}{\Gamma} \oint_{\Gamma} C_{2D}(q_x, q_y) d\gamma = \frac{1}{2\pi} \int_0^{2\pi} C_{2D}(q \cos\psi, q \sin\psi) d\psi \quad (2)$$

In (2), q and ψ are polar variables defined as $q=(q_x+q_y)^{1/2}$, $\psi=\arctan(q_y/q_x)$, and thus $C(q)$ is the average $C_{2D}(q)$ taken over every circumference Γ of radius q and origin $(q_x=0, q_y=0)$. In the case of self-affine surfaces, for which a rescale in the planar coordinates $x \rightarrow bx$ and $y \rightarrow by$ is accompanied by a rescaling in the normal direction $z(b\chi) \rightarrow b^H z(\chi)$, $C(q)$ can be written as

$$C(q) = \frac{H}{2\pi} \left(\frac{h_0}{q_0}\right)^2 \left(\frac{q}{q_0}\right)^{-2(H+1)}, \quad q > q_0 \quad (3)$$

where q_0 is the lower cut-off wavenumber corresponding to an upper cut-off wavelength $\lambda_0=2\pi/q_0$; and h_0 is related to the rms roughness amplitude as $h_0=2^{1/2} R_{rms}$. A self-affine fractal surface can be consequently univocally identified by specifying the surface roughness (R_{rms}), the cut-off wavenumber q_0 and the coefficient H , known as the Hurst coefficient. In a loglog plot, the power spectrum density appears as a line with a slope β for $q > q_0$. The slope β is related to the Hurst parameters as $\beta=2(H+1)$. The fractal dimension D of the surface can be derived from β or H as $D=(8-\beta)/2$ or, equivalently, $D=3-H$. The fractal dimension D for a surface ranges from 2, representing a perfectly flat surface (Euclidean dimension of a surface), to 3, representing an

extremely rough surface. For $D=2.5$, the so-called Brownian surfaces are identified which have totally random and uncorrelated profiles.

Culturing neuroblastoma cells on the substrates. Mouse neuroblastoma (Neuro-2a, N2A) cell line was obtained from the American Type Culture Collection (ATCC). N2A cells were cultured in Dulbecco's Modified Eagle's Medium (DMEM) (Invitrogen, Carlsbad, California), supplemented with 10% fetal bovine serum (FBS, Invitrogen) and 5% penicillin G (100 U/ml) and streptomycin sulfate (100 mg/ml) (Invitrogen). The cells were grown at 37 °C in a humidified 5% CO₂ atmosphere. Sterilized porous Si wafer specimens (15×15 mm approximately) were individually placed into single wells of a 6-well plate (Corning Incorporated). Thereafter, the wafer specimens were washed with phosphate-buffered saline solution (PBS, Invitrogen). The cells were finally seeded in complete cell culture medium and incubated for 24, 36, 48 and 60 h at 37 °C in a humidified 5% CO₂/air atmosphere. After incubation, cell culture medium was removed and the cells were washed twice in PBS and fixed with 4% PFA (paraformaldehyde) and were incubated for 30 min at room temperature (RT). The cells were washed twice PBS and permeabilized with 0.05% triton (Invitrogen) for 5 minutes at RT. All cells fixed and permeabilized were stained with 100 μl DAPI (40, 6-Diamidino-2-phenylindole, Sigma Aldrich) solution for 10 minutes at 4 °C in the dark. Finally, the DAPI solution was removed and each sample was washed with PBS. The total number of cells n_{tot} initially deposited in each well for incubation was approximately $5\sim 10^5$. The cells were sub-confluent throughout the duration of the experiment.

Imaging adhering cells on the substrates. An inverted Leica TCS-SP2® laser scanning confocal microscopy system was used to image cells adhering on the substrates. All measurements were performed using a ArUv laser. The pinhole ($\sim 80 \mu\text{m}$, or equivalently ~ 1.5 Airy units) and laser power (80% power) were maintained throughout each experiment. Confocal images of blue (DAPI) fluorescence were collected using a 405 nm excitation line and a 10× dry objective, so that cells with a characteristic size of a few microns could be clearly observed. For each substrate, a large number of images was taken for statistical analysis. Each image was acquired over a region of interest of $882\times 882 \mu\text{m}^2$ (pixel size $\sim 1.72 \mu\text{m}$) and averaged over 4 lines and 10 frames to improve quality and reduce noise. The images were digitalized into

512×512 pixel and stored on a computer. The fluorescent confocal images of the cells were exported into MatLAB® and Mathematica® for processing.

Network analysis of N2A cells. Confocal images of the cells cultured on the substrates were processed to extract the (i) average *cluster coefficient* and (ii) *characteristic path length* as a function of time, the combination of these parameters gives an indication of the connectivity properties of the cells in a network.

The clustering coefficient (C_c) is a parameter that, in graph theory, gives a measure of the propensity of the nodes of a graph to bundle or cluster together. And thus the extent of gathering of a group of cells may be lumped in the sole global metric parameter C_c : C_c spans from 0 to 1, at the limit of c_c going to 0, the cells are poorly or not connected, when c_c tends to 1, cells group to form a single aggregate. Images were pre-processed using a Gaussian filter to reduce noise and improve image quality. Cell graphs were therefore generated reproducing the spatial distribution of cells as a graph (mesh) of nodes (cells). In this framework, each nucleus (originally stained in blue DAPI) is a node of the network. The existence, occurrence and position of the nodes in this network, and how from these the clustering coefficient may be derived, is described in details in³⁸, and is recapitulated below. In the first place, k-means segmentation algorithms are applied, whereby the original image is partitioned into $\kappa=k$ different segments that gradually transition from bright ($\kappa=1$) to dark ($\kappa=k$). The information content of the image is thus associated to a gray level $\kappa=t$, and all the segments brighter than a certain threshold t , are disregarded as background. The remaining are instead maintained and their value is shifted to 1, and thus the class information for each pixel is presented with black pixels (binary 1) corresponding to the cell class, and with white pixels (binary 0) corresponding to the background class. k and t depend upon the particular problem at study and, for the present configuration, they were set as $k=13$ and $t=7$. The resulting image (g) is therefore down sampled, that is, if f is the average operator, f is shifted over g by steps of size d (and notice that d^2 is the expected area of a nucleus in pixels); in mathematical terms we say that we perform a 2D convolution of f and g , over a regular square grid of size d . The outcome of this is another image where the pixel intensity, ranging from 0 to 1, indicates the probability for a pixel of being a cell. Upon application of another threshold, whereby a grid entry with probability greater than that of the threshold is considered to be a node of the graph, the spatial information of the cells is ultimately translated to their locations in the bi

dimensional grid. The nodes (that are, the cells) are thus organized in the plane as to form a graph (that is, a mesh). The properties of the graph, and particularly the clustering coefficient, may be derived solely if the connections amid the nodes are determined. To do this, the Waxman model is used, whereby the probability of being a link between two nodes exponentially decreases with the Euclidean distance between those nodes³⁸. And thus at each pair of nodes a probability function can be associated being

$$p(u, v) = \alpha e^{-d(u,v)/\beta L} \quad (4)$$

where d is the Euclidean distance between nodes u and v , and L is the largest possible Euclidean distance between two nodes of the grid. In Eq.(4), α and β are the Waxman model parameters and, on tuning these, the graph may be more or less dense. α and β should be chosen between 0 and 1, in a fashion that the network is sufficiently dense to reflect the topology of the system without loss of information. For the present configuration, these parameters were set as $\alpha=1$ and $\beta=0.05$. The probability p varies between 0 for a pair of nodes with an ideally infinite distance, and 1 for a pair of nodes with an ideally zero distance. On the basis of p , the graph can be conveniently reduced, still retaining the information necessary for deriving the clustering coefficient

$$C = \frac{E_i}{n(n-1)/2} \quad (5)$$

where n is number of neighbors of a generic node i , E_i is the number of existing connections between those, being $n(n-1)/2$ the maximum number of connections, or combinations, that can exist among n nodes. Notice that the clustering coefficient c_i is defined locally, a global value, C_c , is derived on averaging c_i over all the nodes that compose the graph.

The Waxman model described above can be used to calculate the characteristic path length (Cpl) of the clusters of N2A cells at any time. The Cpl is a good estimate of the ability of neurons to communicate. It returns the average minimum distance between any pair of nodes in the graph. We shall call here the minimum distance between a generic couple of nodes the shortest path length (Spl), that is expressed as an integer number of steps. The information about the connections among the nodes in a graph is contained in the adjacency matrix $A=a_{ij}$, where the indices i, j run through the number of nodes n in the graph. $a_{ij}=1$ if there exists a connection

between i and j , $a_{ij}=0$ otherwise. In the analysis, *reciprocity* between nodes is assumed, and thus if information can flow from i to j , it can reversely flow from j to i . In the framework of graph theory, we call a similar network an *undirected* graph. Notice that this property translates into symmetry of A being $a_{ij}=a_{ji}$. Moreover, $a_{ii}=0$.

We showed above how to derive the distances between nodes d_{ij} in the networks of N2A cells. On the basis of d_{ij} , we may decide whether a pair of nodes is connected, we use at this end the formula:

$$\alpha e^{-d_{i,j}/\beta L} - R \geq 0 \quad (6)$$

in which R is a randomly generated variable, and the other terms of the Waxman model are defined above in the text. With these premises, we now show how to calculate the Spl for a couple of nodes n_l and n_m . In A , $a_{l,i}$, $a_{i,m}$, account for all the pairs of nodes which are connected to n_l and n_m respectively. The sum of $a_{l,i}$, $a_{i,m}$ over all the nodes in A , $\sum a_{l,i} a_{i,m}$, is stored in a new matrix A_2 for all the l and all the m , and A_2 has the same dimension of A . Now multiply A_2 and A repeatedly $A_2=A_2 \cdot A$ until all the terms of A_2 are non-zero and those terms in position ij will be the Spl between node i and node j . Finally, the characteristic path length Cpl is calculated like the average of Spl over A_2 .

Statistical analysis. All the data are reported as the sample mean \pm the standard deviation (SD). Pair-wise comparisons between means of different groups were performed using a Student t-test (two tailed, unpaired, unpaired) where, for each couple of normally distributed populations, the null hypothesis that the means are equal were verified. Everywhere in the text the difference between two subsets of data is considered statistically significant if the Student t-test gives a significance level P (P value) smaller than 0.05. Multiple comparisons were performed using an univariate analysis of variance (ANOVA). ANOVA provides a statistical test of whether or not the means of several groups are all equal, and therefore generalizes the Student t-test to more than two groups. ANOVA was used here for comparing more than two means.

Acknowledgments

This work has been partially funded from the EU Commission, the European Social Fund and the Calabria Region (POR Calabria FSE 2007-2013) and from the Italian Minister of Health under the project “Cancer biomarker detection using micro-structured/super-hydrophobic surfaces and advanced spectroscopy techniques” (Project n. GR-2010-2320665).

References

1. E. Kandel, J. Schwartz and T. Jessell, *Principles of Neural Science*, McGraw-Hill, New York, 2000.
2. M.-H. Kim, M. Park, K. Kanga and I. S. Choi, *Biomaterials Science*, 2014, **2**, 148–155.
3. J. P. Crutchfield, *Nature Physics*, 2012, **8**, 17-24.
4. J. J. Hopfield, *Proc. Nat. Acad. Sci. USA*, 1982, **79**, 2554-2558.
5. S. H. Strogatz, *Nature*, 2001, **410**, 268-276.
6. <https://www.humanbrainproject.eu/>.
7. B. Geiger, A. Bershadsky, R. Pankov and K. M. Yamada, *Nature Reviews, Molecular Cell Biology*, 2001, **2**, 793-805.
8. B. Geiger, J. P. Spatz and A. D. Bershadsky, *Nature Reviews, Molecular Cell Biology*, 2009, **10**, 21-33.
9. P. Kanchanawong, G. Shtengel, A. M. Pasapera, E. B. Ramko, M. W. Davidson, H. F. Hess and C. M. Waterman, *Nature*, 2010, **468**, 580-586.
10. A. Ferrari, M. Cecchini, A. Dhawan, S. Micera, I. Tonazzini, R. Stabile, D. Pisignano and F. Beltram, *Nano Letters*, 2011, **11**, 505–511.
11. S. Ankam, M. Suryana, L. Y. Chan, A. A. K. Moe, B. K. K. Teo, J. B. K. Law, M. P. Sheetz, H. Y. Low and E. K. F. Yim, *Acta Biomaterialia*, 2013, **9**, 4535–4545.
12. E. Migliorini, J. Ban, G. Greci, L. Andolfi, A. Pozzato, M. Tormen, V. Torre and M. Lazzarino, *Biotechnology and Bioengineering*, 2013, **110**, 2301-2310.
13. P. Roach, T. Parker, N. Gadegaard and M. R. Alexander, *Surface Science Reports*, 2010, **65**, 145-173.
14. R. Sorkin, A. Greenbaum, M. David-Pur, SaritAnava, A. Ayali, E. Ben-Jacob and Y. Hanein, *Nanotechnology*, 2009, **20**, 015101.

15. C. Xie, L. Hanson, W. Xie, Z. Lin, B. Cui and Y. Cui, *Nano Letters*, 2010, **10**, 4020–4024.
16. K. Baranes, N. Chejanovsky, N. Alon, A. Sharoni and O. Shefi, *Biotechnology and Bioengineering*, 2012, **109**, 1791- 1797.
17. E. Migliorini, G. Greci, J. Ban, A. Pozzato, M. Tormen, M. Lazzarino, V. Torre and M. E. Ruaro, *Biotechnology and Bioengineering*, 2011, **108**, 2736-2746.
18. A. A. K. Moe, M. Suryana, G. Marcy, S. K. Lim, S. Ankam, J. Z. W. Goh, J. Jin, B. K. K. Teo, J. B. K. Law, H. Y. Low, E. L. K. Goh, M. P. Sheetz and E. K. F. Yim, *Small*, 2012, **8**, 3050–3061.
19. T. Gabaya, E. Jakobsa, E. Ben-Jacobb and Y. Hanein, *Physica A*, 2005, **350**, 611–621.
20. Z. Huangab and X. Jiang, *Journal of Materials Chemistry C*, 2013, **1**, 7652–7662.
21. M. Kwiat, R. Elnathan, A. Pevzner, A. Peretz, B. Barak, H. Peretz, T. Ducobni, D. Stein, L. Mittelman, U. Ashery and F. Patolsky, *ACS Applied Materials and Interfaces*, 2012, **4**, 3542–3549.
22. T. Limongi, F. Cesca, F. Gentile, R. Marotta, R. Ruffilli, A. Barberis, M. D. Maschio, E. M. Petrini, S. Santoriello, F. Benfenati and E. Di Fabrizio, *Small*, 2013, **9**, 402–412.
23. Y. Sun, Z. Huang, K. Yang, W. Liu, Y. Xie, B. Yuan, W. Zhang and X. Jiang, *Plos ONE*, 2011, **6**, e28156.
24. M. Tang, Q. Song, N. Li, Z. Jiang, R. Huang and G. Cheng, *Biomaterials*, 2013, **34**, 6402-6411.
25. F. Gentile, R. L. Rocca, G. Marinaro, A. Nicastrì, A. Toma, F. Paonessa, G. Cojoc, C. Liberale, F. Benfenati, E. Di Fabrizio and P. Decuzzi, *ACS Applied Materials and Interfaces*, 2012, **4**, 2903–2911.
26. Y. L. Khung, G. Barritt and N. H. Voelcker, *Experimental Cell Research*, 2008, **314**, 789–800.
27. H. Foll, M. Christophersen, J. Carstensen and G. Hasse, *Materials Science and Engineering*, 2002, **39**, 93–141.
28. F. Gentile, E. Battista, A. Accardo, M. Coluccio, M. Asande, G. Perozziello, G. Das, C. Liberale, F. De Angelis, P. Candeloro, P. Decuzzi and E. Di Fabrizio, *Microelectronic Engineering*, 2011, **88**, 2537-2540.

29. Y. Hu, A. Bouamrani, E. Tasciotti, L. Li, X. Liu and M. Ferrari, *ACS Nano*, 2010, **4**, 439–451.
30. H. H. P. Yiu and P. A. Wright, *Journal of Materials Chemistry*, 2005, **15**, 3690–3700.
31. S. Godefroo, M. Hayne, M. Jivanescu, A. Stesmans, M. Zacharias, O. I. Lebedev, G. V. Tendeloo and V. V. Moschalkov, *Nature Nanotechnology*, 2008, **3**, 174-178.
32. J. S. Ananta, B. Godin, R. Sethi, L. Moriggi, X. Liu, R. E. Serda, R. Krishnamurthy, R. Muthupillai, B. R. D. L. Helm, M. Ferrari, L. J. Wilson and P. Decuzzi, *Nature Nanotechnology*, 2010, **5**, 815-821.
33. M. Gaspari, M. M.-C. Cheng, R. Terracciano, X. Liu, J. Nijdam, L. Vaccari, E. Di Fabrizio, E. F. Petricoin, L. A. Liotta, G. Cuda, S. Venuta and M. Ferrari, *Journal of Proteome Research*, 2006, **5**, 1261-1266.
34. R. Terracciano, M. Gaspari, F. Testa, L. Pasqua, P. Tagliaferri, M. M.-C. Cheng, J. Nijdam, E. F. Petricoin, L. A. Liotta, G. Cuda, M. Ferrari and S. Venuta, *Proteomics*, 2006, **6**, 3243-3250.
35. F. Gentile, M. Monteferrante, L. Chiodo, A. Toma, M. L. Coluccio, G. Ciccotti and E. Di Fabrizio, *Molecular Physics: An International Journal at the Interface Between Chemistry and Physics*, 2014, **112**, 1375-1388.
36. F. Gentile, L. Tirinato, E. Battista, F. Causa, C. Liberale, E. Di Fabrizio and P. Decuzzi, *Biomaterials*, 2010, **31**, 7205-7212.
37. C. Demir, S. H. Gultekin and B. Yener, *Bioinformatics*, 2005, **21**, 7-12.
38. C. Gunduz, B. Yener and S. H. Gultekin, *Bioinformatics*, 2004, **20**, 145-151.
39. M. E. J. Newman, *SIAM Rev*, 2003, **45**, 167–256.
40. C. J. Thiele, in *J. Human Cell Culture*, ed. Masters, Kluwer Academic Publishers, Lancaster, UK, 1998, vol. 1, pp. 21-53.
41. D. J. Watts, *Small Worlds: The Dynamics of Networks between Order and Randomness*, Princeton University Press, Woodstock, 2003.
42. D. J. Watts and S. H. Strogatz, *Nature*, 1998, **393**, 440-442.
43. L. A. N. Amaral, A. Scala, M. Barthélemy and H. E. Stanley, *Proc. Nat. Acad. Sci. USA*, 2000, **97**, 11149–11152.
44. V. Latora and M. Marchiori, *Physical Review Letters*, 2001, **87**, 198701.

45. S. Achard, R. Salvador, B. Whitcher, J. Suckling and E. Bullmore, *the Journal of Neuroscience*, 2006, **26**, 63-72.
46. D. S. Bassett and E. Bullmore, *Neuroscientist*, 2006, **12**, 512-523.
47. E. Bullmore and O. Sporns, *Nature Reviews Neuroscience*, 2012, **13**, 336-349.
48. C. Moore and M. E. J. Newman, *Physical Review E*, 2000, **61**, 5678.
49. L. F. Lago-Fernández, R. Huerta, F. Corbacho and J. A. Sigüenza, *Physical Review Letters*, 2000, **84**, 2578.
50. F. Comellas, J. Ozóná and J. G. Peters, *Information Processing Letters*, 2000, **76**, 83–90.
51. N. Takahashi, T. Sasaki, W. Matsumoto, N. Matsuki and Y. Ikegaya, *Proc. Nat. Acad. Sci. USA*, 2010, **107**, 10244–10249.
52. A. Borst and F. E. Theunissen, *Nature Neuroscience*, 1999, **2**, 947 – 957.
53. S. P. Strong, R. Koberle, R. R. d. R. van Steveninck and W. Bialek, *Physical Review Letters*, 1998, **80**, 197.
54. K. Friston, *Nature Reviews Neuroscience*, 2010, **11**, 127-138.
55. G. M. Wang, E. M. Sevick, E. Mittag, D. J. Searles and D. J. Evans, *Physical Review Letters*, 2002, **89**, 050601-050604.
56. R. Linsker, *Neural Computation*, 1997, **9**, 1661-1665.
57. V. J. Kiselev, K. R. Hahn and D. P. Auerc, *NeuroImage*, 2003, **20**, 1765–1774.

Figure Legends

Figure 1 Schematic of the work. PSi substrates were generated from a bulk boron-doped p-type (100) silicon wafer via anodization. The original silicon wafer was placed in a Teflon electrolytic cell, where a platinum cathode and the silicon wafer (anode) are immersed in a hydrogen fluoride (HF) solution (**a-b**). PSi substrates were therefore obtained with an average pore size spanning the MeP and MaP regimes (**c**). In culturing neuroblastoma N2A cells on similar substrates (**d**), we found that the surface topography influences the assembly of those cells into complex networks, which may be described by the sole clustering coefficient and characteristic path length (**e**).

Figure 2 The morphology of the macro porous silicon film is revealed in high resolution SEM micrographs with an increasing magnification factor ranging from 10 000 × (**a**), to 20 000 × (**c**),

to $100\ 000 \times$ (d). (b) is a cross sectional SEM image of the macro porous substrate from which one can deduce the thickness t of the porous matrix that, for the present configuration, is about $t \sim 250$ nm. (e) is an ultra-high magnification image of the inset in (d). This and other similar images can be used to estimate the pore size distribution in the upper porous surface (i), where the average pore size is $S \sim 75$ nm the standard deviation is $\sigma \sim 5$ nm. Atomic Force Microscopy (AFM) was used to characterize the porous surface even further. AFM 2d (f) and 3d (g) images reveal the topography of the pores over a region of 500 nm per side. These images were therefore processed and used to derive the power spectrum density function C of the substrate, in which the change in the information content of the image is reported as a function of spatial frequency in a log log diagram. The slope of C in the region of the diagram in which it is linear, is proportional to the fractal dimension D_f that for the present surface preparation reads as $D_f \sim 2.7$. The macro porous silicon chips are hydrophobic with a contact angle $\theta \sim 120^\circ$, for convenience, they were processed in an oven at high temperature $T = 290^\circ\text{C}$ and rendered hydrophilic with a final contact angle $\theta \sim 35^\circ$.

Figure 3 Characterization of the MeP silicon substrates. Ultra high resolution SEM micrographs of the samples reveal the porous structure at the smallest scales for the SP (a) and LP (c) MeP configurations. From these, using standard image analysis algorithms, the pore size distribution (g) and thus the average pore sizes may be determined that are $S \sim 8$ nm, for the SP MeP substrate, and $S \sim 18$ nm, for the LP MeP substrate. The samples were further analyzed using AFM imaging. The AFM profiles of the SP (b) and LP (e) MeP surfaces were processed to obtain the corresponding power spectrum (PS) density functions (c,f), which permitted to evaluate the characteristic fractal dimensions of the porous surfaces being $D_f \sim 2.8$ for the SP MeP architecture, and $D_f \sim 2.5$ for the LP MeP architecture. Contact angle measurements of the samples upon heating show that the substrates are rendered hydrophilic with a contact angle of $\theta \sim 30^\circ$ (h) that is similar to that derived for the MaP architecture.

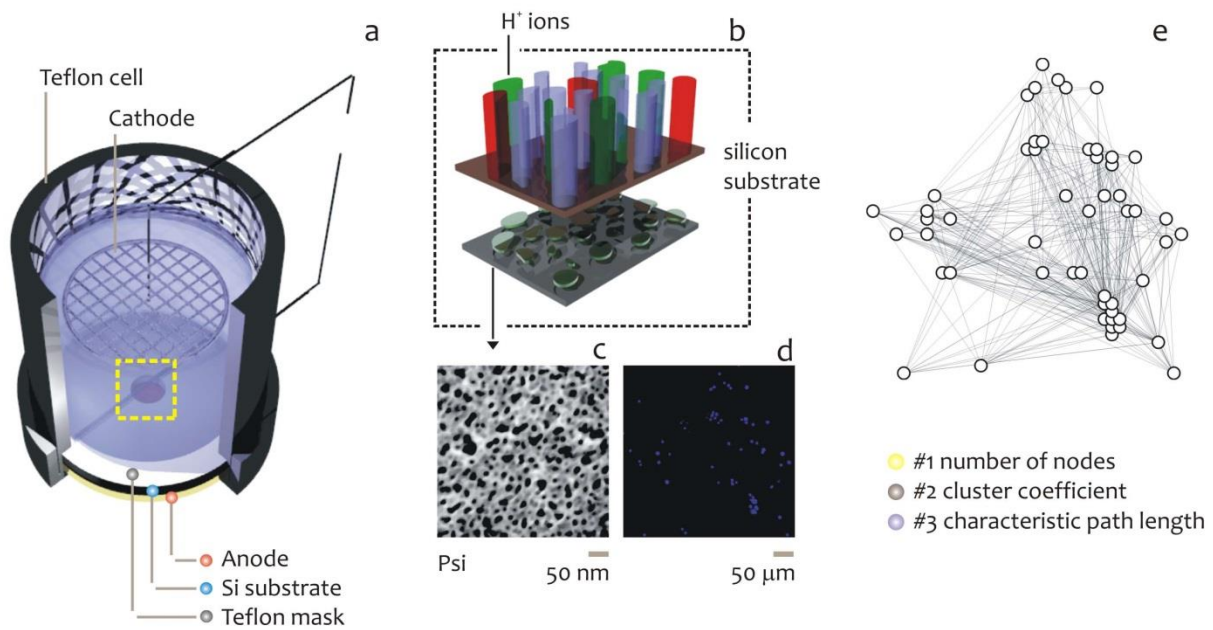
Figure 4 The macro-porous silicon surfaces were used as a substrate for N2A cell culture. Neural cells were incubated over the porous silicon chips and the number of adhering cells was measured over time. (a) indicates the number of adhering cells as a function of time, compared to the cells in adhesion on a flat silicon substrate used as a control, the same information is reported

in (b) as a function of substrate preparation. Both diagrams indicate that macro porous surfaces improve cell adhesion and proliferation.

Figure 5 DAPI confocal images of N2A cells 36 h after incubation are reported in (a) for a flat silicon surface and in (d) for a MaP silicon substrate. The topology of those cells in a plane is revealed by the corresponding graphs (b-e) that are a simplified pictorial representation of the nuclei of the cells (which are, the nodes) and the signal connections between those cells (which are, the edges), that were calculated using the Waxman model described in the Materials and Methods. The distribution of the number of edges that you may find at different nodal distances is reported in the histograms in (c-f), these are single-peaked in the flat silicon case and double peaked in the macro porous silicon case, and this reflects the fact that cells are randomly distributed in the plane in the first instance (with an average cell distance that corresponds to the single peak of the distance distribution), and form groups of cells in the second instance (where the two peaks correspond to the intra and inter group distances).

Figure 6 a statistical analysis permitted to derive the clustering coefficient C_c (a) and the characteristic path length C_{pl} (b) of the networks of N2A cells the flat and porous silicon substrates for all the considered times of the analysis. The diagrams demonstrate that cells on a porous surface display high clustering and short paths in contrast to cells on a continuous smooth surface (minor differences in the position between groups of cells on the porous surfaces can be ascribed to the different fractal structure of MaP, SP and LP MeP silicon, that is reflected by their fractal coefficients that are, respectively, $D_f \sim 2.7$, $D_f \sim 2.8$, $D_f \sim 2.5$, and that are generally larger than that revealed by flat silicon, that is $D_f \sim 2.3$). The definition and significance of the clustering coefficient and of the characteristic path length are provided separately in the Materials and Methods and throughout the paper.

Figure 7 a to d are the scatter plots of the C_c and C_{pl} of networks of N2A cells on a flat silicon surface and the porous silicon surfaces at different time frames. They permit to visualize the different effects of the described surfaces on cell networking at a glance. The scheme in (e) divides or categorizes classes of different graphs on the basis of the C_c and C_{pl} solely: differently from regular lattices or random graphs, small world graphs have high clustering and short paths. Cells on porous silicon films reveal the characteristics of a small world network.

**Figure 1**

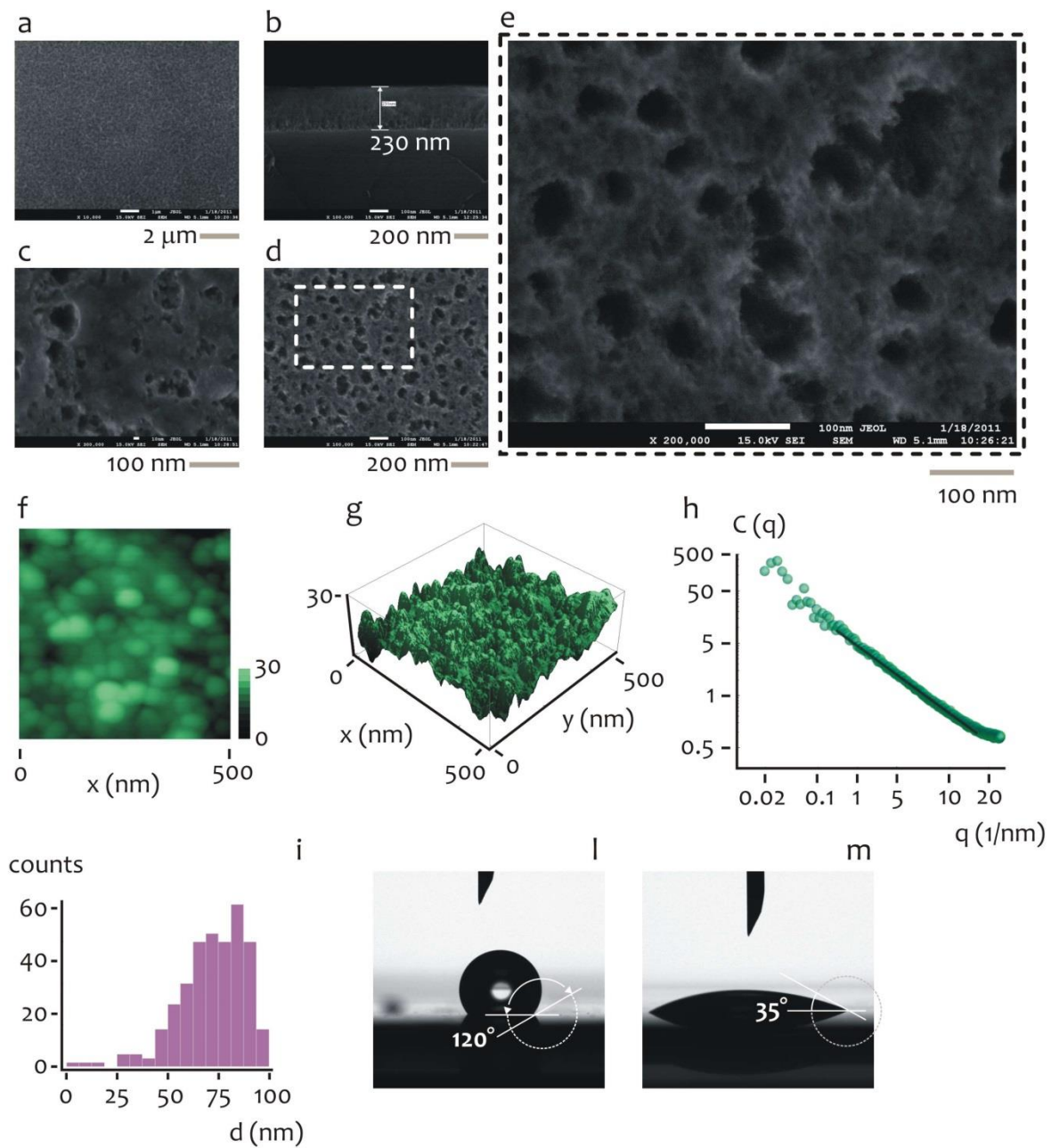


Figure 2

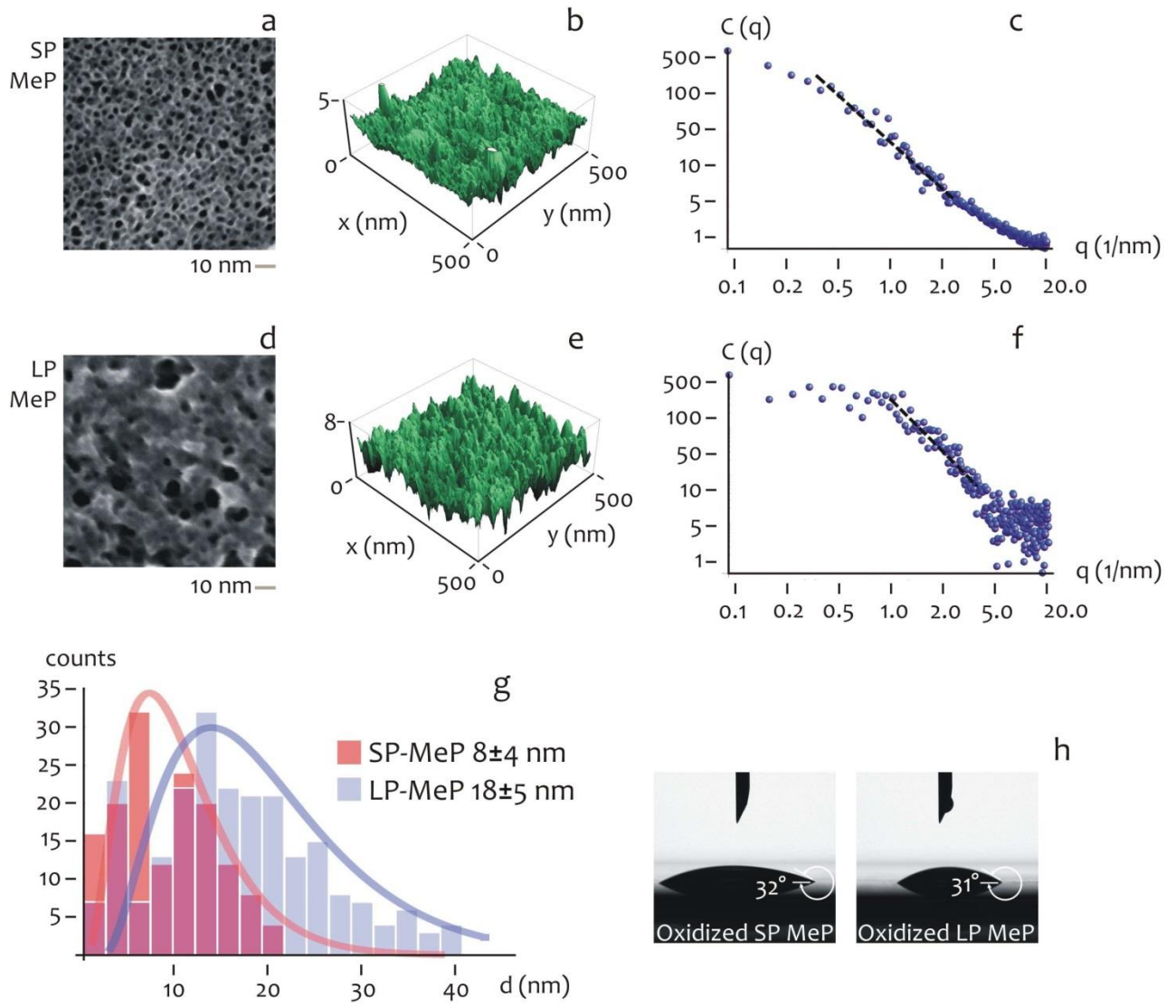


Figure 3

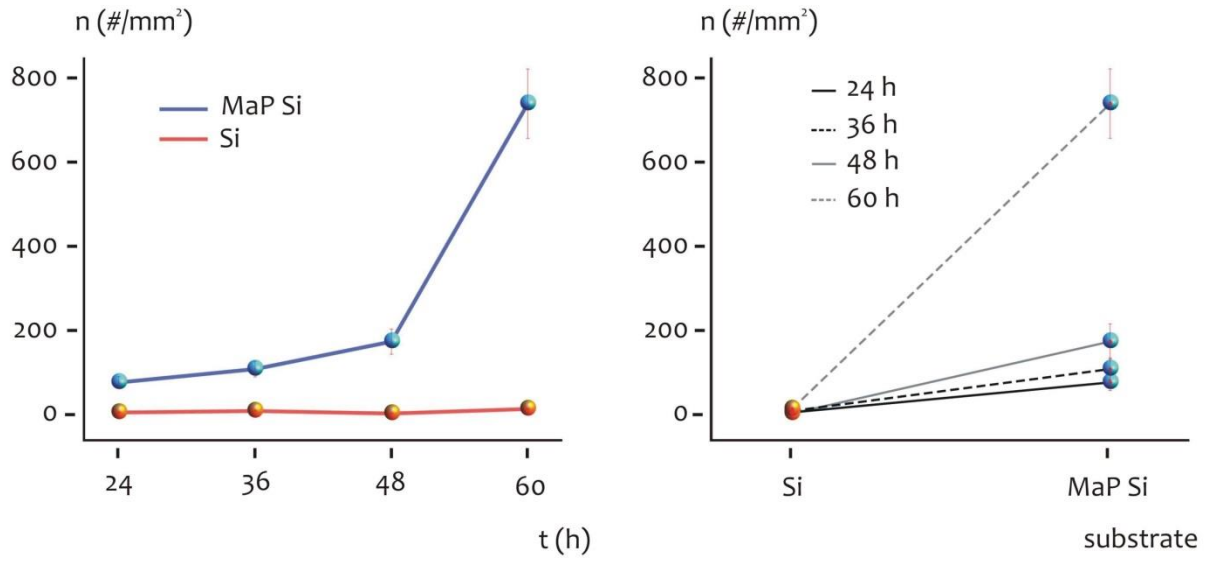


Figure 4

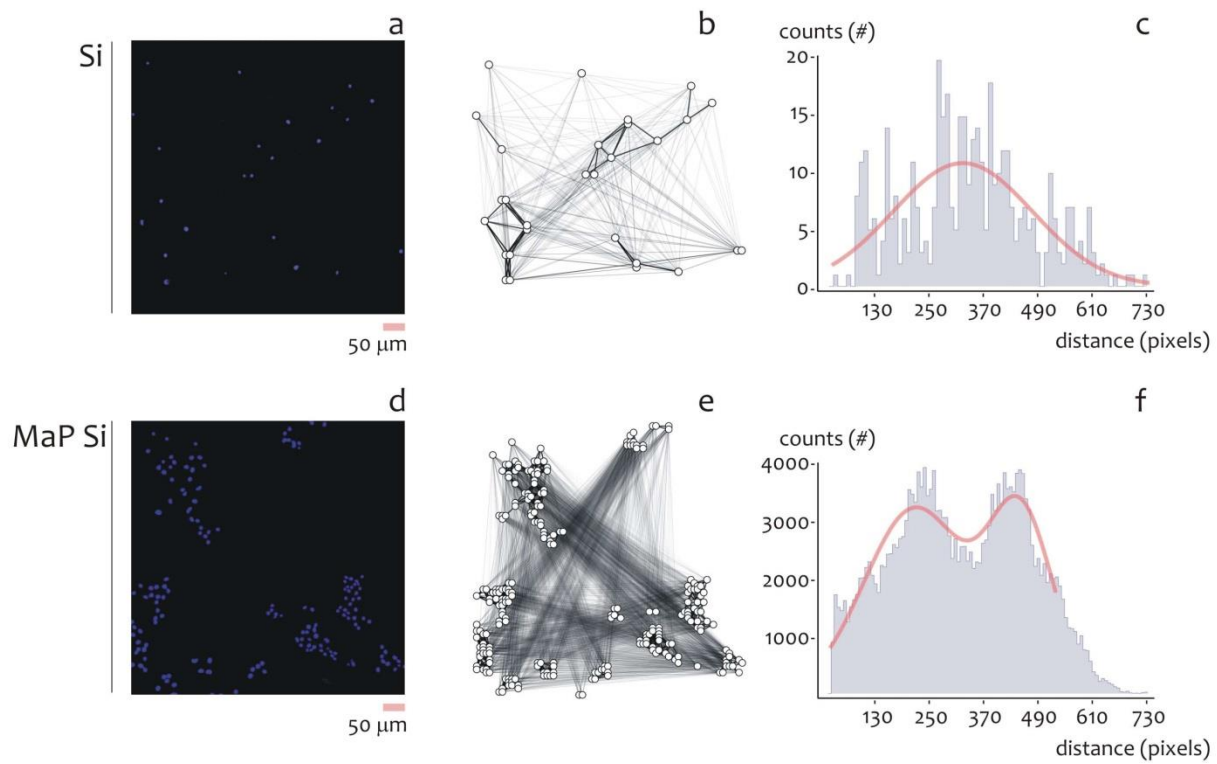


Figure 5

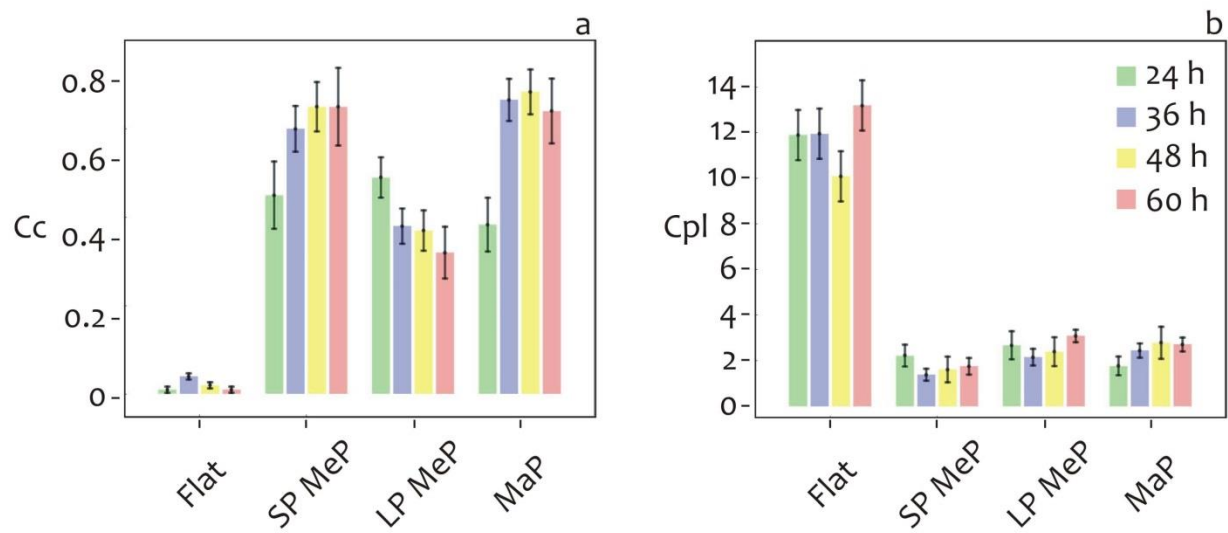


Figure 6

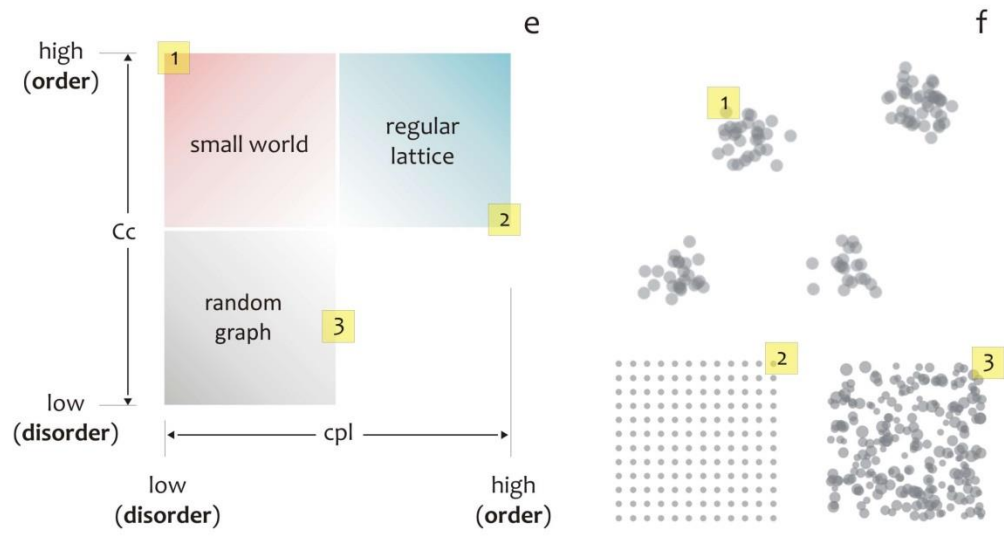
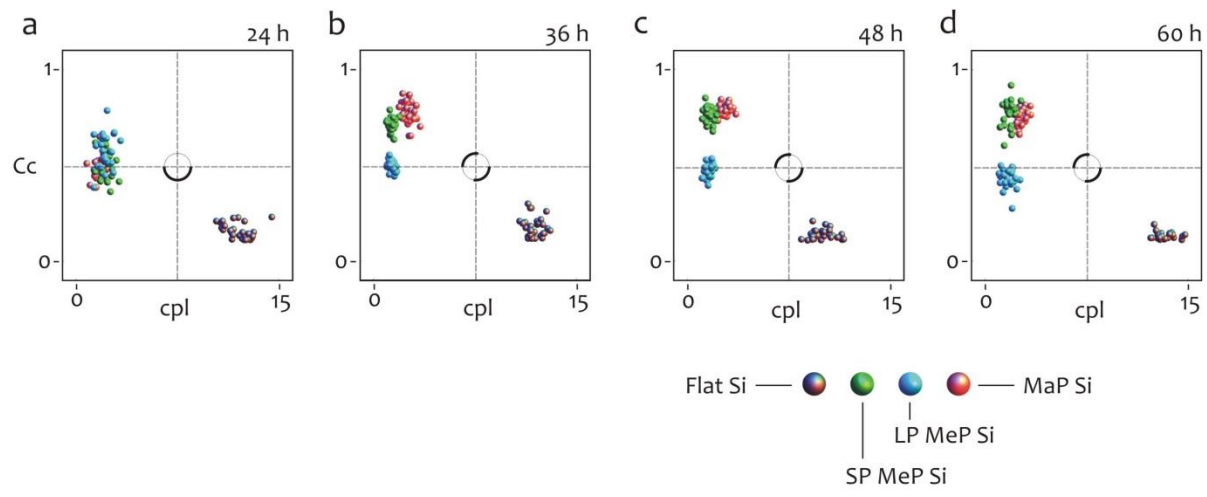


Figure 7